

# Monitoring temporal opacity fluctuations of large structures with muon tomography: a calibration experiment using a water tower\*

Kevin Jourde<sup>1</sup>, Dominique Gibert<sup>2,3,\*</sup>, Jacques Marteau<sup>4</sup>, Jean de Bremond d'Ars<sup>2</sup>, Serge Gardien<sup>4</sup>, Claude Girerd<sup>4</sup>, and Jean-Christophe Ianigro<sup>4</sup>

<sup>1</sup>Institut de Physique du Globe de Paris (CNRS UMR 7154), Sorbonne Paris Cité, Paris, France.

<sup>2</sup>OSUR - Géosciences Rennes (CNRS UMR 6118), Université Rennes 1, Rennes, France.

<sup>3</sup>National Volcano Observatories Service, Institut de Physique du Globe de Paris (CNRS UMR 7154), Paris, France.

<sup>4</sup>Institut de Physique Nucléaire de Lyon, Univ Claude Bernard (UMR 5822 CNRS), Lyon, France.

\*gibert@univ-rennes1.fr

## ABSTRACT

Usage of secondary cosmic muons to radiography the density distribution of geological structures significantly developed during the past ten years. Recent applications demonstrate the interest of the method to monitor magma ascent and volcanic gas movements inside volcanoes. Muon radiography could be used to monitor density variations in aquifers and the critical zone in the near surface. However, the time-resolution achievable by muon radiography monitoring remains poorly studied, and the aim of the present study is to document this issue. We present a muon radiography monitoring of water level variations in a water tower; conditions are similar to those expected for the near surface. Data are used to discuss the influence of atmospheric variability that perturb the signal. We propose correction formulas to extract variations of the muon flux related to changes of water level. Statistical developments establish the feasibility domain of muon radiography monitoring as a function of target thickness (i.e. opacity). Objects with a thickness comprised between  $\approx 50 \pm 30$  m water equivalent correspond to the best time-resolution. Thinner objects have a degraded time-resolution that strongly depends on the zenith angle, thicker objects like volcanoes have a time-resolution that does not depend on the zenith angle.

## Introduction

Using the muon component of secondary cosmic rays to radiography geological bodies like volcano lava domes is the subject of increasing interest over the past ten years. Much like medical X-ray radiography, muon radiography aims at recovering the density distribution,  $\rho$ , inside the targets by measuring their screening effect on the natural flux of cosmic muons. This approach was first tested by Alvarez et al.<sup>1</sup> who tried to radiography the Egyptian Pyramid of Chephren to eventually find a hidden chamber. The method then stayed long dormant until recent years when, thanks to progress in electronics and particle detectors, field instruments were designed and constructed by several research teams worldwide. Muon radiography experiments have successfully been performed on volcanoes where the hard muon component is able to cross several kilometres of rock<sup>2–10</sup>. Applications to civil engineering (tunnels, dams) and environmental studies (near surface geophysics) are subject to active research, and monitoring of density changes in the near surface constitutes an important objective in hydrology and soil sciences.

The main property that can be recovered with muon radiography is the opacity,  $\varrho$ , which quantifies the amount of matter encountered by the muons along their path,  $L$ , across the target,

$$\varrho = \int_L \rho(l) \times dl. \quad (1)$$

Generally, the opacity is expressed in  $[\text{g.cm}^{-2}]$  or, equivalently, in centimetres water equivalent  $[\text{cm.w.e.}]$ . Muons lose their energy through matter by ionisation processes<sup>11</sup> and the loss of energy is typically 2.5 MeV for an opacity of 1  $\text{g.cm}^{-2}$ . Muons are relativistic leptons produced in the upper atmosphere, at an altitude of about 16 km<sup>12,13</sup>, and they reach the ground after losing about 2.5 GeV to cross the opacity of 10 m.w.e. represented by the atmosphere. Muons travel along straight trajectories across low-density materials, including water, concrete and rocks. Scattering is significant, whatever the muon

momentum, only in high-density materials like lead and uranium<sup>11</sup>. However, low-energy muons ( $E \leq 1$  GeV) have strong scattering in almost all materials.

Muon radiography of kilometre-size objects like volcanoes involves the hard muonic component with energy above several hundredths of GeV. In such cases, the incident flux of muons may reasonably be considered stationary, azimuthally isotropic and to only depend on the zenith angle<sup>5;12</sup>. The situation is quite different for targets with a low opacity of several m.w.e. that can be crossed by the soft muonic component (i.e. several GeV). Contrarily to the hard component, the flux of low-energy muons can no more be considered stationary and isotropic. Atmospheric effects<sup>14</sup>, and to a lesser extend geomagnetic effects<sup>15;16</sup>, are considered to be the main causes of non-stationarity and anisotropic characteristics of the soft muon component<sup>12;13</sup>.

The low-energy component of the primary flux (up to 4 GeV) mostly comes from the sun<sup>17</sup> and is modulated by coronal mass ejections (CME) that depend on the 11-years solar cycle. Although the duration of the solar cycle is too long to be detected by a muon radiography monitoring, individual CME and the resulting geomagnetic disturbances may produce transient perturbations of the soft muon component. These muons are stopped by opacities larger than 16 m.w.e. For these reasons, muon radiography monitoring of targets with an opacity of only several m.w.e is a difficult challenge that deserves further assessment and methodological developments.

The present study is a contribution to the assessment of muon radiography monitoring of low-opacity target. In the remaining, we present a controlled experiment performed on a water tank tower whose opacity fluctuates in a significant range ( $3 \text{ m.w.e.} < \varrho < 5 \text{ m.w.e.}$ ) where atmospheric effects are expected to significantly perturb the flux of incident cosmic muons. Measurements are made during a period of several weeks while the opacity remains steady at its maximum level before fluctuating. Meanwhile, water level in the tank, atmospheric pressure, and geomagnetic activity are monitored in order to evaluate their relative importance to produce variations of the flux of muons measured across the water volume.

In the remaining we first present the SHADOW experiment during which the flux of muons crossing the water tank is measured. The analysis of the data follows with an estimate of the atmospheric effects producing variations of the flux of muons. Finally, a discussion of the time resolution in muon radiography monitoring is presented with a particular emphasis for the case of low-opacity targets.

## The SHADOW experiment

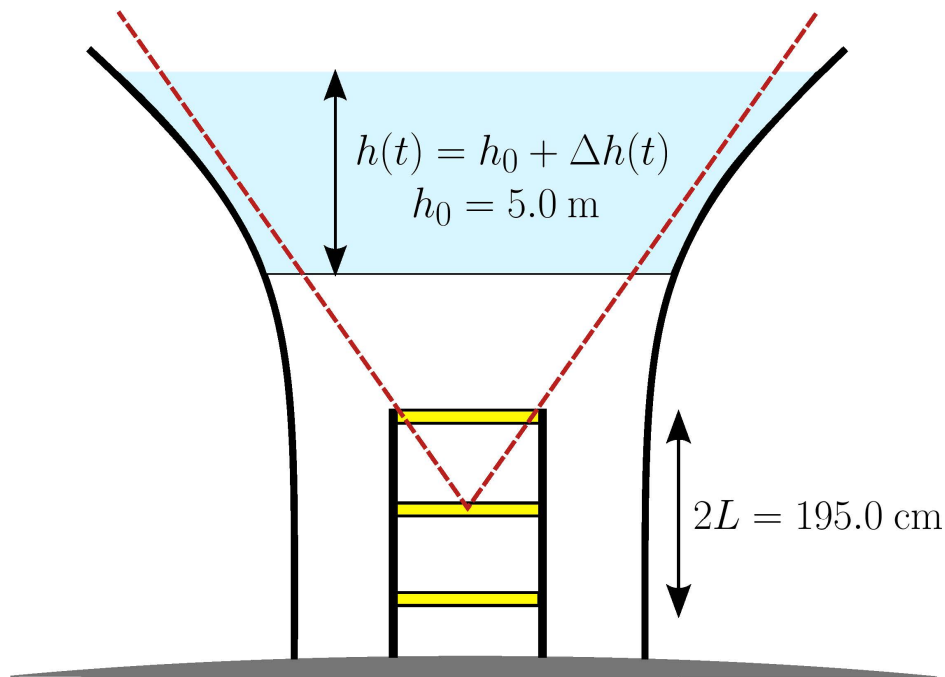


**Figure 1.** Sketch of the SHADOW experiment. The three yellow rectangles are the detection matrices (each with  $16 \times 16$  pixels of  $5 \times 5 \text{ cm}^2$ ), the red dotted lines encompass the detection solid angle and the blue surface represents the water volume.

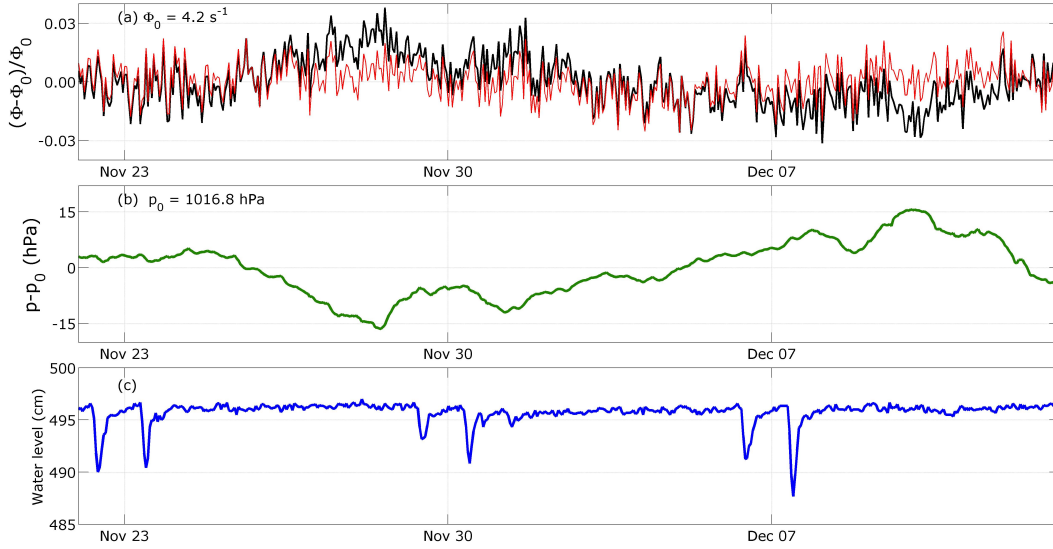


**Figure 2.** Hourly means of the data acquired during the calibration period (November 22<sup>th</sup> to December 13<sup>th</sup>, 2014): **(a)** Relative time-variation of the muon flux (black curve) and muon flux corrected from the atmospheric pressure influence (red curve). **(b)** time-variation of the atmospheric pressure relative to  $p_0 = 1016.8$  hPa. **(c)** Variation of the water level.

The SHADOW experiment measured the time-variations of the muonic component while the water level varied in a water tower. For this purpose, a muon telescope (a description is given in the Methods Section below) was placed on the symmetry axis of the tower and below the tank. The instrument was oriented vertically (i.e. central zenith angle = 0) as shown in Figure 1 so that the apparent opacity is only function of the zenith angle (azimuthal invariance) and of time when the water level  $h(t)$  is changing. The water tower is located in Tignieu-Jamezieu, France, a village located 20 kilometres East from Lyon (altitude 230 m above sea level,  $X_{UTM} = 31\,669\,490$ ,  $Y_{UTM} = 5067\,355$ ). The distance between the upper and the lower matrices is set at 195 cm to cover a zenith angle range  $0^\circ \leq \theta \leq 22.3^\circ$  such that all 961 lines of sight of the telescope pass through the water. The solid angle spanned by the telescope equals  $\Omega_{\text{int}} = 0.161$  sr, and the total effective acceptance  $\mathcal{T}_{\text{int}} = 630$  cm<sup>2</sup>sr.

The data acquisition started on November 21<sup>th</sup>, 2014 and stopped on January 22<sup>th</sup>, 2015. While measuring the flux of muons crossing the tank, the water level was monitored with an accuracy of several cm every 5 minutes by the company in charge of the tower (Syndicat Intercommunal des Eaux de Pont-de-Ch  ruy – SIEPC). These data are completed by hourly measurements of the atmospheric pressure at the nearby Saint Exup  ry airport located less than 5 km away from the water tower.

In the next section, we use hourly means of these data series to document the relationship between the time-variations of the muon flux and those of both the atmospheric pressure and the water level in the water tower.

### Constant water level: Evaluation of atmospheric effects

We first consider the data acquired during the first three weeks of the measurement period, from November 22<sup>th</sup> to December 13<sup>th</sup> 2014, when the water level in the water tower remained almost constant at its maximum level  $h_0 = 496$  cm (Figure 2c). Meanwhile, the atmospheric pressure varied by  $\pm 15$  hPa with respect to a reference pressure  $p_0 = 1016.8$  hPa (Figure 2b). The flux of muons shown on Figure (2a) not only randomly fluctuates as expected for a Poissonian process but also contains long-period variations with an amplitude of less than 3%. These long-period variations are clearly anti-correlated with those of the atmospheric pressure (Figure 2b).

Since the water level is mainly constant during the considered period, we expect that the time variations of the muon flux are principally due to atmospheric effects. The graph in Figure 3 represents the hourly-averages of the muon flux with respect to the hourly values of the atmospheric pressure from Saint Exup  ry airport. In this graph, only the data points such that the water level  $495 \text{ cm} \leq h \leq 496 \text{ cm}$  are retained. A least-squares fit to these points gives a negative slope  $\beta_p = -0.0012$  (0.0001) hPa<sup>-1</sup> where the value in parenthesis is the half-width of the 95% confidence interval. The fit was performed by assigning to the relative flux averages a standard deviation  $\sigma_\Phi = 0.0081$  derived from the statistics of the event arrival times. A standard deviation  $\sigma_p = 1$  hPa is assigned to the atmospheric pressure data. The standard deviation of the residuals of the linear fit,  $\sigma_r = 0.0093$ , falls near  $\sigma_\Phi$  and indicates that no higher-order fit is required. Consequently, in the remaining, we shall represent

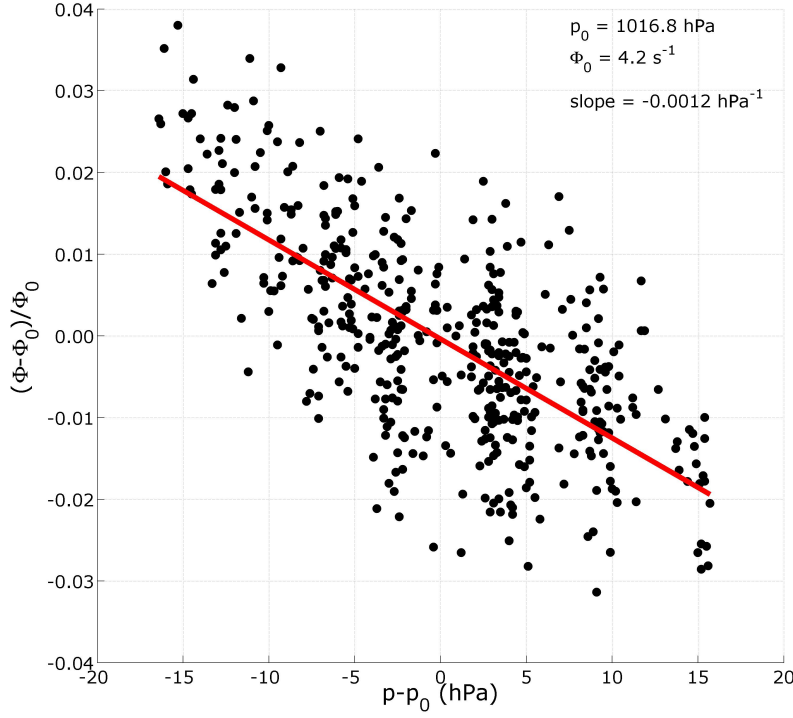


**Figure 3.** Relative variation of the measured muon flux versus atmospheric pressure deviation. The red line represents the best least-squares fit solution. Only the data points corresponding to a water level greater than 495 cm have been kept to compute the line fit.

the atmospheric influence on the relative muon flux with a linear relationship,

$$\frac{\Phi - \Phi_0}{\Phi_0} = \beta_p \times (p - p_0). \quad (2)$$

Dayananda<sup>18</sup> uses the same kind of linear relation and finds  $\beta_p = -0.0013$  (0.0002)  $\text{hPa}^{-1}$  from muon counts at the Earth's surface. Other authors<sup>19;20</sup> also find linear relationships with coefficients falling near  $\beta_p = -0.001 \text{ hPa}^{-1}$ .

The correction formula (2) says that a  $\Delta p = 10 \text{ hPa}$  increase of the atmospheric pressure induces a relative muon flux decreases of 1.2%. Applying this correction to the muon flux data (black curve of Figure 2a) efficiently reduces the long-period variations (light red curve of Figure 2a).

### Time-varying water level

We now consider the data acquired during the second part of the measurement period where large variations of the water level are observed (Figure 4). The considered period begins on December 13<sup>th</sup> 2014 and ends on January 22<sup>th</sup> 2015. The largest decrease in the water level is up to nearly 200 cm with respect to  $h_0$  (Figure 4c). During the same period, the variations of the muon flux appear clearly anti-correlated with the water level (Figure 4b), and the highest relative flux deviation reaches 15% when the water level is minimum ( $\approx 320 \text{ cm}$ ). Meanwhile, the atmospheric pressure variations (Figure 4a) also produce conspicuous effects on the muon flux like, for instance, the flux bump that occurs around December 28<sup>th</sup> during a low-pressure event.

The circles in Figure 5 represent the muon flux data versus the water level. Applying the atmospheric correction (2) to the muon flux reduces the scattering of the data points and enhances the correlation between the flux and the water level (black dots in Figure 5).

A linear fit to the pressure-corrected points is represented by the red line in Figure 5 with a negative slope  $\beta_h = -0.0009$  (0.00002)  $\text{cm}^{-1}$  and an intercept  $\Delta\Phi_w = 0.444$  (0.007). The standard deviations assigned to the water level and muon flux are respectively  $\sigma_h = 1.7 \text{ cm}$  and  $\sigma_\Phi = 0.0082$ . The standard deviation of the residuals,  $\sigma_r = 0.011$ , is not reduced when fitting a second-order polynomial, and we adopt a linear relationship to represent the influence of the water level on the muon flux,

$$\frac{\Phi - \Phi_0}{\Phi_0} = \beta_h \times h + \Delta\Phi_w. \quad (3)$$

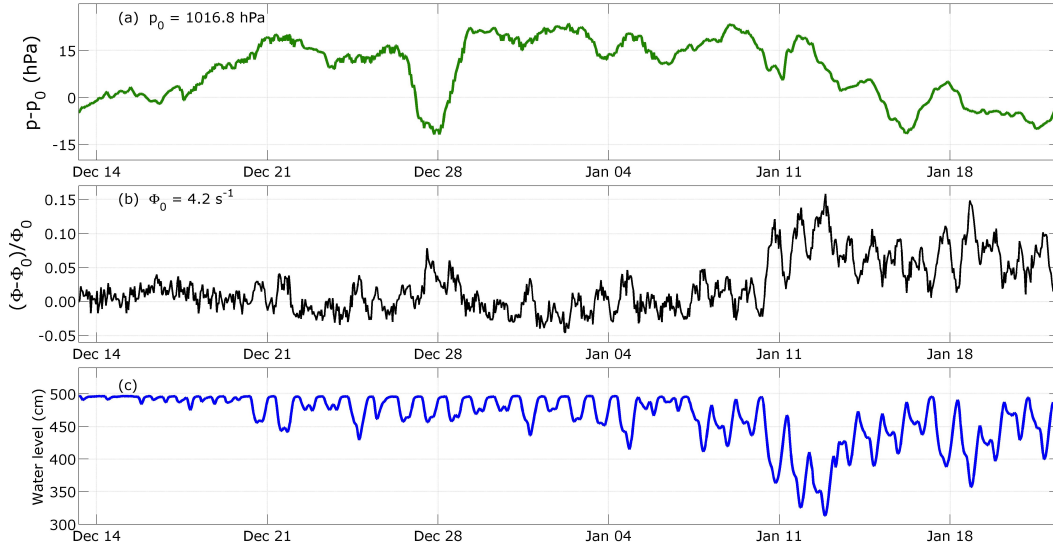


**Figure 4.** Data acquired during the non-stationary period (December 13<sup>th</sup> 2014 to January 22<sup>th</sup> 2015): **(a)** Time-variations of the atmospheric pressure relative to  $p_0 = 1016.8$  hPa. **(b)** Variation of the relative muon flux corrected from the atmospheric pressure influence using the parameters derived from the data of the calibration period. **(c)** Time-variations of the water level.

## Discussion of SHADOW data analysis

The data analysed in the previous Section show that linear relationships (equations 2 and 3) may safely be used to represent the dependence of the relative muon flux with respect to variations of the atmospheric pressure (Figure 3) and of the water level (Figure 5). Owing to the fact that the variations of opacity produced by  $\Delta p = 1$  hPa and  $\Delta h = 1$  cm are identical (i.e. they represent the same mass of matter), it may be deduced that the  $\beta$  coefficients in equations (2) and (3) should be the same. This hypothesis is not supported by our experimental results which indicate that  $\beta_p$  is significantly larger than  $\beta_h$ .

The discrepancy between the experimental values for  $\beta_p$  and  $\beta_h$  is explained by the fact that the atmosphere is not only, like water in the tank, a screen of matter for the muon flux but it is also the place where muons originate<sup>12;13;21</sup>. Consequently, the flux of muons at ground level will depend on both the pressure and the temperature profiles in the atmosphere. For instance, if the atmosphere is warmer, the muon production altitude is higher (roughly at the isobaric level  $p = 100$  hPa) and the transit time of muons increases. Then, muons are more likely to decay before reaching the ground and the relative flux of muons also decreases<sup>12;21</sup>. This is the so-called negative temperature effect. However, an increase in temperature at the production level diminishes the air density, thus reducing the likelihood of pion interactions before their decay into muons. Muon production then increases, and this phenomena is known as the positive temperature effect. Both the pressure and temperature effect upon the flux of muons at ground level may be summarized by<sup>22;23</sup>,

$$\frac{\Phi - \Phi_0}{\Phi_0} = \beta_p^* \times (p - p_0) + \beta_T^* \times (T - T_0), \quad (4)$$

where  $T$  is the temperature at the production level and  $\beta_p^*$  and  $\beta_T^*$  are adjustable coefficients for the pressure and temperature effects respectively. The coefficient  $\beta_p^*$  is always negative while  $\beta_T^*$  may be either positive or negative depending on the prevailing temperature effect. For the soft muon component ( $\leq 10$  GeV) which composes the main part of the particles detected by our telescope, the negative temperature effect dominates and  $\beta_T^*$  is expected to be negative. The correlation analysis recently performed by Zazian et al.<sup>24</sup> shows that the pressure and temperature effects are positively correlated. Consequently, for the measurement conditions of the present study, both  $\beta_p^*$  and  $\beta_T^*$  are negative and time-correlated. When considering the atmospheric effect alone like in equation (2), the  $\beta_p$  coefficient actually accounts for both the pressure and temperature effects. This explain why the experimental value found for  $\beta_p$  (2) is larger than the value of  $\beta_h$  (3).

## Statistical feasibility and limits of opacity monitoring

We now address some statistical issues concerning the monitoring of opacity variations like those produced by water-level variations measured during the SHADOW experiment.

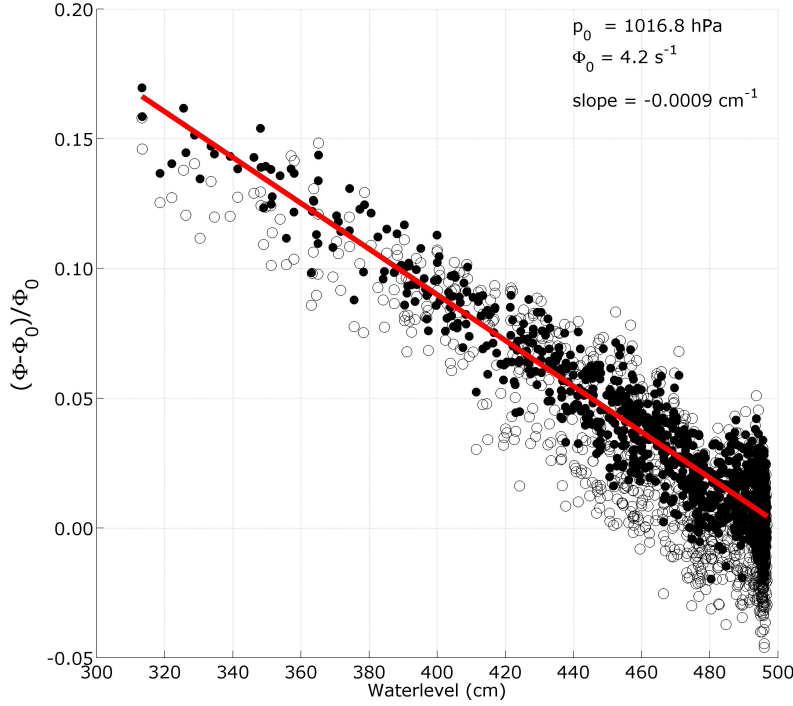


**Figure 5.** Normalized and centred muon flux as a function of water level. The open circles correspond to the measured muon flux (i.e. black curve in Figure 4b) and the black dots correspond to the muon flux corrected from the atmospheric pressure influence (equation 2). The red straight line is the theoretical flux as a function of the water level computed using the theoretical muon absorption law into water (from the Particle Data Group tables).

Let us assume that  $N = N_1 + N_2$  particles are detected by the telescope during a time period  $T$ , and where  $N_1$  and  $N_2$  are the number of particles respectively counted during the first and second half of  $T$ . We want to determine under which conditions  $N_1$  and  $N_2$  may be considered different at the confidence level  $\alpha$ . The particle flux difference  $\Delta N = N_2 - N_1$  obeys a Skellam distribution defined as the difference between two Poisson processes with means  $\mu_1$  and  $\mu_2$ <sup>25</sup>,

$$\mathcal{S}(\Delta N, \mu_1, \mu_2) = e^{-(\mu_1 + \mu_2)} \left( \frac{\mu_1}{\mu_2} \right)^{k/2} I_{\Delta N}(2\sqrt{\mu_1 \mu_2}), \quad (5)$$

where  $I_{\Delta N}$  is the modified Bessel function of the first kind.

In the case where  $N_2 > N_1$ , the hypothesis  $\Delta N \neq 0$  may be considered true at the confidence level  $\alpha$  if

$$\sum_{i=-\infty}^{-1} \mathcal{S}(i, N_1, N_2) + \frac{1}{2} \times \mathcal{S}(0, N_1, N_2) \leq 1 - \alpha \quad (6)$$

$$N_1 = T/2 \times \phi_1 = T/2 \times \phi_0 \times (1 - \varepsilon/2) \quad (7)$$

$$N_2 = T/2 \times \phi_2 = T/2 \times \phi_0 \times (1 + \varepsilon/2). \quad (8)$$

When the inequality (6) becomes an equality we get  $T = T_{min}$ , the minimum acquisition time necessary to resolve a flux difference given by the following set of parameters  $(\phi_0, \varepsilon, \alpha)$ . When  $\varepsilon$  is fixed,  $T_{min}$  is the best time resolution achievable to observe temporal relative variation of the flux larger than  $\varepsilon$ . When  $T_{min}$  is fixed, we derive the best relative flux variation,  $\varepsilon$ , detectable on a time-scale larger than  $T_{min}$ .

Note that if  $(N_1, N_2) \gtrsim 10$  the Poisson laws can be approximated with Gaussians and equation (6) is simplified to,

$$(N_2 - N_1) - \tilde{\alpha} \times \sqrt{\frac{N_1 \times N_2}{N_1 + N_2}} \geq 0 \quad (9)$$

$$T \geq T_{min} = \frac{\tilde{\alpha}^2 (1 - \varepsilon^2/4)}{\varepsilon^2 \times \phi_0} \quad (10)$$

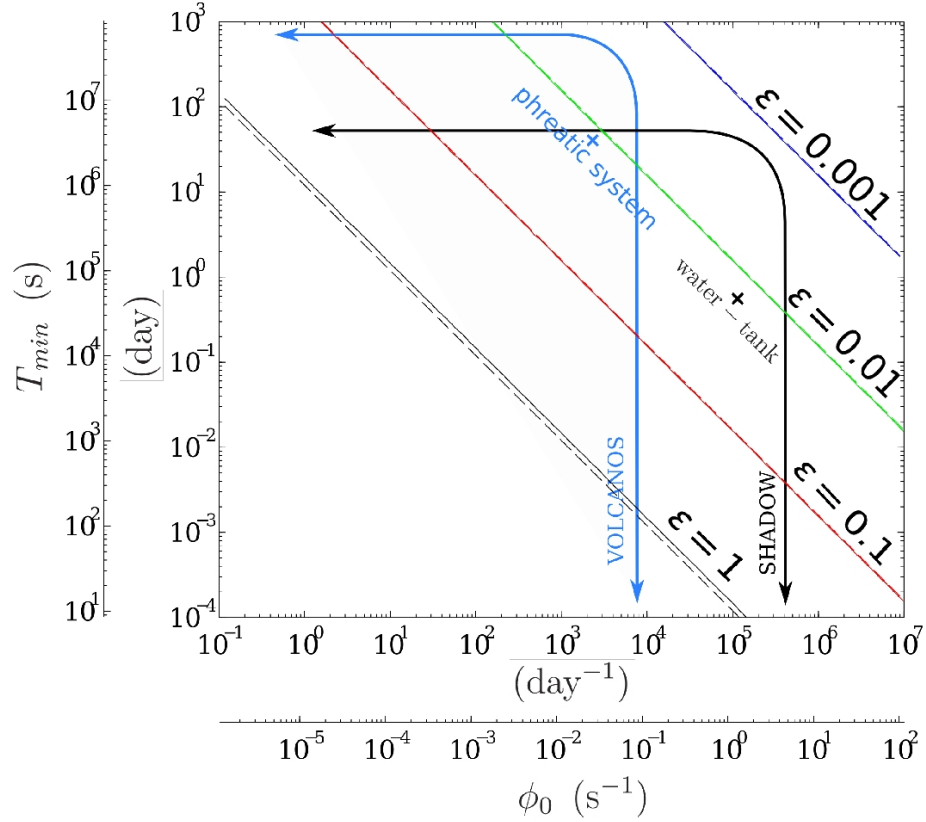


**Figure 6.** Minimum acquisition time  $T_{min}$  versus the average measured flux  $\phi_0$  necessary to detect a relative variation of flux of  $\alpha$  at the 95% confidence level. The straight and dotted lines are the iso- $\alpha$  curves respectively computed with equation (6) and the approximation (10). The curved arrows delimit the resolution domains for the SHADOW experiment and typical volcano applications. The horizontal limit marked by the arrows is the measurement whole duration and the vertical limit is the maximum flux measured. The crosses represent likely sources of variations of the muon flux, their coordinates depend on the flux fluctuations amplitude  $\alpha$  and their typical period  $T_{min}$ .



where  $\alpha = \text{erf}(\tilde{\alpha})$ .

We numerically compute  $T_{min}$  from equation (6) with a confidence level  $\alpha = 0.05$  and represent it on Figure 6 for a range of measured muon flux and variation threshold  $\varepsilon = 1, 0.1, 0.01$ , and  $0.001$  (i.e. 100%, 10%, 1%, and 0.1%). Observe that the approximation (10) is suitable for our range of applications,  $T_{min}$  will be underestimated starting from  $\varepsilon \gtrsim 0.5$  which implies  $N \approx 20$ .

Figure 6 shows that to detect a daily variation in the count of muons of 2% ( $\varepsilon = 0.02$ ), as is typically observed in the SHADOW experiment, an average flux  $\phi_0 > 2 \text{ s}^{-1}$  must be measured. This solution is represented by the black cross labelled "water tank" on Figure 6. The lower-left domain delimited by the curved black arrow in Figure 6 represents the solution-domain for time-scales and opacity variations of the SHADOW experiment category. This solution-domain is the region where flux variations can be resolved at a high confidence level. The horizontal branch of the arrow is limited by the duration of the measurement period, and the vertical branch is placed at a level corresponding to the maximum flux that can be measured by the telescope. This latter quantity may be augmented by increasing the acceptance of the telescope either by augmenting the angular aperture (i.e. by reducing the distance between the detection matrices), by grouping several lines of sight, or by using detectors with a larger area.

The feasibility domain for a typical volcano experiment is also represented on Figure 6 and delimited by the blue curved arrow. Note that for this kind of experiments we have a longer acquisition time and a tiny measured flux as the total opacity of the geological body facing the telescope is much bigger than for the SHADOW experiment: about 1000 m.w.e. for a volcanic lava dome versus 5 m.w.e. for the water-tank.

We can rewrite equation (6) into a form more suitable for tomography applications by replacing the flux fluctuations by opacity fluctuations,

$$N = T \times \phi(\mathcal{T}, \varrho_0, \theta) \quad (11)$$

$$N_1 = T/2 \times \phi(\mathcal{T}, \varrho_0 \times (1 - \varepsilon/2), \theta) \quad (12)$$

$$N_2 = T/2 \times \phi(\mathcal{T}, \varrho_0 \times (1 + \varepsilon/2), \theta), \quad (13)$$

where the muon flux  $\phi$ , is explicitly written to depend on telescope acceptance  $\mathcal{T}$ , opacity  $\varrho_0$ , and zenith angle  $\theta$ . As before,  $\varepsilon$  represents the variation of opacity relative to the average opacity  $\varrho_0$ . We warn the reader that a given  $\varepsilon$ -variation of  $\varrho$  corresponds to a much larger  $\varepsilon$ -variation of  $\phi$ . Putting equations (12) and (13) in equation (9) we obtain the following feasibility condition,

$$T \geq T_{min}(\varrho_0, \varepsilon, \theta, \mathcal{T}) = \frac{2 \times \tilde{\alpha}^2 \times \phi_1 \times \phi_2}{(\phi_2 - \phi_1)^2 \times (\phi_2 + \phi_1)} \quad (14)$$

where  $T_{min}$  is the minimum duration of the measurement period necessary to resolve the sought opacity variation. Note that the feasibility formula from Lesparre et al.<sup>5</sup> is the first order development of equation (14).

A subset of  $T_{min}$  solutions of equation (14) is represented on Figure 7 for the confidence level  $\alpha = 0.05$ , for zenith angles  $\theta = 0^\circ, 30^\circ$ , and  $60^\circ$ , and opacity variations  $\varepsilon = 100\%, 10\%, 1\%$ . An acceptance,  $\mathcal{T} = 10 \text{ cm}^2 \cdot \text{sr}$ , typical of our telescopes has been used in the calculus. Roughly, a variation of  $\varepsilon$  by an order of magnitude induces a change of  $T_{min}$  by two orders of magnitude.

Observe that there is an optimal opacity range where the measurement time, i.e. the time resolution that is achievable, is minimum to resolve a given opacity variation. The optimal opacity range depends on the zenith angle and goes roughly from 40 to 100 m.w.e for  $\theta = 0^\circ$ , and from 20 to 40 m.w.e for  $\theta = 60^\circ$ . For low-opacity conditions, measurements at high zenith angles are wise to optimize the time-resolution. This is particularly conspicuous for the SHADOW experiment where the average opacity  $\varrho_0 \approx 5 \text{ m.w.e}$  and  $\varepsilon \approx 10\%$ . For these parameters, Figure 7 gives  $T_{min} > 1 \text{ day}$  is necessary at  $\theta = 0^\circ$  to resolve the fluctuations while  $T_{min} > 0.2 \text{ day}$  is sufficient at  $\theta = 60^\circ$ . This strong dependence of the time-resolution with respect to the zenith angle disappears at larger opacities  $\varrho_0 > 500 \text{ m.w.e}$  like those encountered in volcano muon tomography.

## Discussion

Muon radiography offers an interesting mean to monitor opacity/density variations inside geological bodies. Noticeable advantages of the method are the possibility to remotely radiography unapproachable dangerous volcanoes and to image the density distribution of large volumes from a single view-point<sup>6,8,26</sup>. Muon tomography is entering an era of precision measurements not only for structural imaging but also for dynamical monitoring purposes. Some monitoring experiments have been performed on active volcanoes that demonstrate the usefulness of such measurements to constrain the evolution of eruption crisis<sup>10</sup>. However, as shown above, monitoring opacity variations is subject to both statistical and experimental constraints that limit the resolution that can be achieved. Understanding these limits is of a primary importance to improve the method and to assess the validity of muon radiography monitoring.



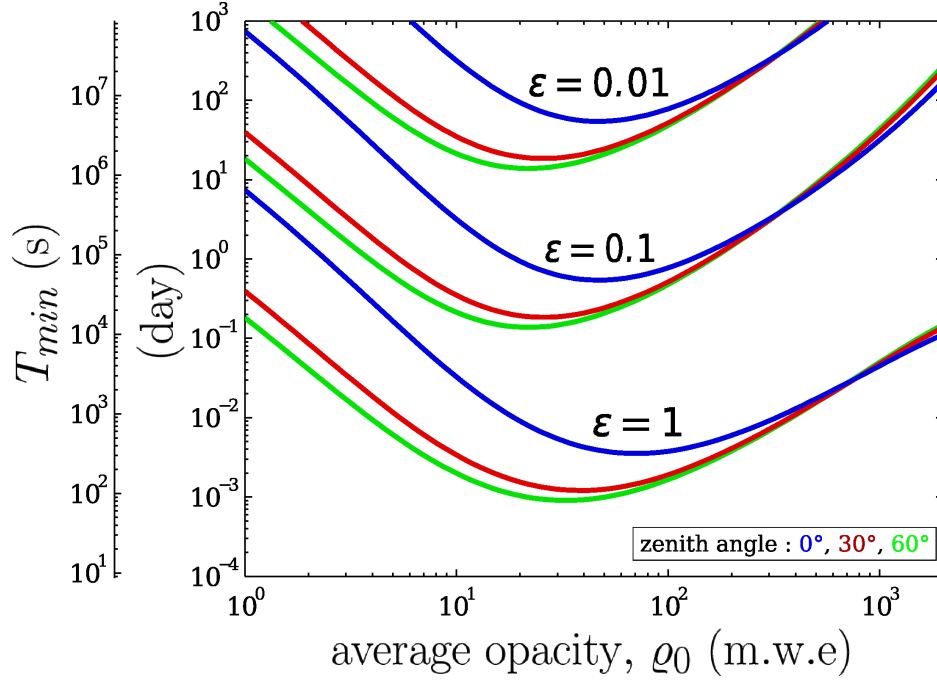


**Figure 7.** Minimum acquisition time  $T_{min}$  as a function of the average opacity  $\rho_0$  to detect an  $\varepsilon$  fluctuation at the  $\alpha = 0.05$  confidence level. The three curves (resp. blue, red, green) correspond to three different observation zenith angles (resp.  $0^\circ$ ,  $30^\circ$ ,  $60^\circ$ ) and are computed for  $\mathcal{T} = 10 \text{ cm}^2 \cdot \text{sr}$  using the modified Gaisser model from Tang et al (2006).

Experimental constraints are partly dictated by statistical considerations, and mainly come from the telescope acceptance that limits the maximum flux which fixes the right boundary of the resolution domain in Figure 6). This boundary may be moved rightward by increasing the acceptance  $\mathcal{T}$  of the instrument. Recalling that  $\mathcal{T}$  is expressed in  $[\text{cm}^2 \text{sr}]$ , the acceptance may be augmented by several means: 1) increasing the solid angle encompassed by the instrument by reducing the distance between the detection matrices; 2) increasing the detection surface by coupling several telescopes (actually our telescopes may be merged into a single one); 3) grouping lines of sight to increase both the detection surface and the solid angle at the price of reducing the angular resolution of the radiographies. In the present study, the latter solution has been retained and all lines of sight have been merged to obtain an effective acceptance of  $630 \text{ cm}^2 \text{sr}$ .

Statistical constraints bound the resolution domain of a given experiment (Figure 6), and the main concern when doing measurements is to ensure that the phenomena to monitor fall inside the boundaries. As will be discussed in the next paragraph, the telescope configuration may be adapted to comply with the objectives of the ongoing experiment. As shown in the preceding sections, the statistical constraints are quite different whether the opacity is high or low. This is conspicuous in Figure (7) where the feasibility solutions for  $T_{min}$  strongly differ in the low- and high-opacity domains. It is remarkable that variations of high-opacities are equally resolved whatever the zenith angle while, instead, the resolution for low-opacities strongly depends on this angle. Another conspicuous feature present in Figure (7) is the existence of an optimal medium-opacity range  $\rho \approx 50 \pm 30 \text{ m.w.e.}$  where telescopes offer their best performance. The existence of this optimal range of opacity comes from the nature of the cosmic muon energy spectrum<sup>12;27;28</sup>, and changing the acceptance of the telescope has no effect on the optimal opacity values but only changes  $T_{min}$  by translating the solution curves of Figure (7) either upward (decrease of acceptance) or downward (augmentation of acceptance).

## Methods

The muon count series analysed in the present study were acquired with one of our standard telescopes shown in Figure 8<sup>8;29;30</sup>. The picture was taken during an open-sky calibration phase where the muon count serves to determine the efficiency of the scintillator bars forming the detection matrices. Each matrix is formed by an assemblage of two sets of 16 bars arranged perpendicularly obtain an array of  $16 \times 16$  square pixels of  $5 \times 5 \text{ cm}^2$ . The upper and lower matrices of the telescope allow  $31 \times 31$  combinations of pixels, i.e. 961 distinct lines of sight. The distance between the matrices may be changed to adapt the solid angle spanned by the trajectories. In the present study, the distance was tuned to encompass the entire water tank (Figure 1).



**Figure 8.** Picture of the muon telescope used for the SHADOW experiment, here during the open-sky calibration phase. The three detection matrices are horizontal. The calibration gives access to the effective acceptance and allows to measure the timing parameters for the time-of-flight measurements. The control box embedding a mini-PC, a common clock distribution system, a network switch is visible on the middle matrix.

Once geometrically configured, the telescope is totally characterised by its acceptance function  $\mathcal{T}_i$  [ $\text{cm}^2\text{sr}$ ] which relates the muon count,  $N_i$ , to the flux of cosmic muons,  $\partial\phi$  [ $\text{s}^{-1}\text{cm}^{-2}\text{sr}^{-1}$ ] received by the telescope in its  $i^{\text{th}}$  line of sight,

$$N_i = T \times \int_{4\pi} \mathcal{P}_i(\varphi, \theta) \times \partial\phi(\varrho, \varphi, \theta) \times d\Omega, \quad (15)$$

$$= T \times \mathcal{T}_i \times \partial\phi_i, \quad (16)$$

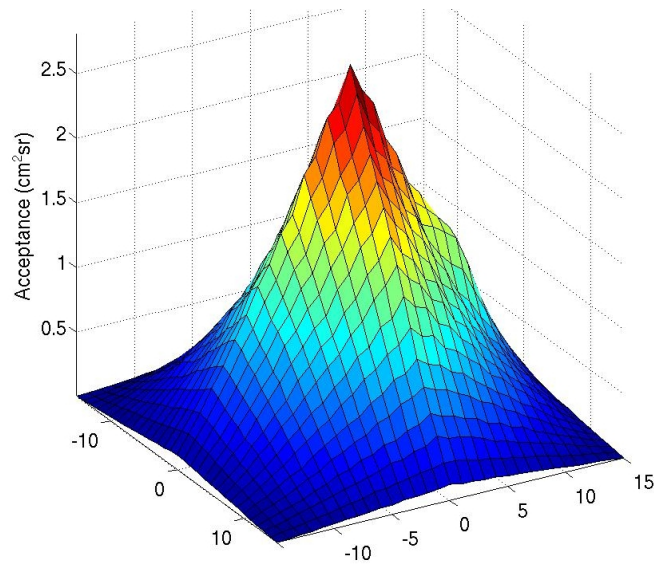
where  $T$  is the duration of the acquisition period,  $\mathcal{P}_i$  [ $\text{cm}^2$ ] is the detection surface function of the line of sight,  $\mathcal{T}_i$  is the integrated acceptance, and  $\partial\phi_i$  is the muon flux in the central direction of the line of sight. It must be understood that  $\partial\phi$  [ $\text{s}^{-1}\text{cm}^{-2}\text{sr}^{-1}$ ] is the differential flux of muons that actually reaches the instrument after crossing the target. Consequently,  $\partial\phi$  depends both on the open sky differential flux  $\partial\phi(\varrho = 0, \varphi, \theta)$  and on the muon absorption law inside matter. These are determined through experiments<sup>19;20;27;31–34</sup>, theoretical works<sup>28</sup> or thanks to Monte-Carlo simulations<sup>35;36</sup> depending on the precision expected and the available information.

Figure (9) shows the acceptances  $\mathcal{T}_i$  for  $i = 1, \dots, 961$  of the telescope used in the SHADOW experiment. This acceptance function is determined experimentally to account for the defects of the detection matrices, mainly imperfect optical couplings at the output of the scintillator bars and on the face of the multichannel photomultiplier. These defects are the causes of the distortions visible in the 3D plot of Figure (9). In practice, the determination of the acceptance is performed by measuring the flux of muons coming from the zenith and under the open sky.

The number of detected particles  $N$  may be increased by grouping several adjacent lines of sight belonging to a subset  $\mathcal{E}$ ,

$$N_{\mathcal{E}} = T \times \sum_{i \in \mathcal{E}} \mathcal{T}_i \times \partial\phi_i = \sum_{i \in \mathcal{E}} N_i. \quad (17)$$

This results in an augmentation of the corresponding acceptance and to a better time-resolution. The counterpart is a degradation of the angular resolution induced by the merging of the small solid angles spanned by the trajectories. In the present study, the entire solid angle spanned by the telescope trajectories were grouped to obtain a total acceptance  $\mathcal{T}_{\text{total}} = 630 \text{ cm}^2\text{sr}$ . Such a large acceptance dramatically improves the time-resolution which falls to the order of tens of minutes in the case of the SHADOW experiment.



**Figure 9.** Experimental acceptance of the telescope for the configuration shown in Figure (1). The maximum value of the acceptance,  $\mathcal{T}_{\max} = 2.80 \text{ cm}^2\text{sr}$  is obtained for the line of sight perpendicular to the detector planes and corresponding to  $(x, y) = (0, 0)$ . The  $x$  and  $y$  coordinates represent the horizontal offsets between the pixels defining a given line of sight of the telescope (one pixel in the upper detection matrix, and the other one in the lower matrix). The acceptance integrated over the entire surface of the detectors equals  $\mathcal{T}_{\text{int}} = 630 \text{ cm}^2\text{sr}$  for a solid angle aperture of  $\Omega_{\text{int}} = 0.161 \text{ sr}$ .

## References

1. Alvarez, L. *et al.* Search for hidden chambers in the pyramids. *Science* **167**, 832–839 (1970).
2. Nagamine, K. Geo-tomographic observation of inner-structure of volcano with cosmic-ray muons. *J. Geogr.* **104**, 998–1007 (1995).
3. Tanaka, H. *et al.* Development of the cosmic-ray muon detection system for probing internal-structure of a volcano. *Hyperfine Interact.* **138**, 521–526 (2001).
4. Tanaka, H., Nagamine, K., Nakamura, S. & Ishida, K. Radiographic measurements of the internal structure of mt. west iwaite with near-horizontal cosmic-ray muons and future developments. *Nucl. Instrum. Methods* **A555**, 164–172 (2005).
5. Lesparre, N. *et al.* Geophysical muon imaging: feasibility and limits. *Geophys. J. Int.* **183**, 1348–1361 (2010).
6. Lesparre, N. *et al.* Density muon radiography of la soufriere of guadeloupe volcano: comparison with geological, electrical resistivity and gravity data. *Geophys. J. Int.* **190**, 1008–1019 (2012).
7. Marteau, J. *et al.* Muons tomography applied to geosciences and volcanology. *Nucl. Instrum. Methods* **A695**, 23–28 (2012).
8. Jourde, K. *et al.* Experimental detection of upward going cosmic particles and consequences for correction of density radiography of volcanoes. *Geophys. Res. Lett.* **40**, 6334–6339 (2013).
9. Portal, A. *et al.* Inner structure of the puy de dôme volcano: cross-comparison of geophysical models (ert, gravimetry, muon imaging). *Geosci. Instrum. Method Data Syst.* **2**, 47–54 (2013).
10. Tanaka, H. K., Kusagaya, T. & Shinohara, H. Radiographic visualization of magma dynamics in an erupting volcano. *Nature* **5** (2014).
11. Nagamine, K. *Introductory muon science* (Cambridge University Press, 2003).
12. Gaisser, T. K. *Cosmic rays and particle physics* (Cambridge University Press, 1990).
13. Grieder, P. K. *Cosmic rays at Earth* (Gulf Professional Publishing, 2001).

14. Yanchukovsky, V., Filimonov, G. Y. & Hisamov, R. Atmospheric variations in muon intensity for different zenith angles. *Bull. Russ. Acad. Sci. Phys.* **71**, 1038–1040 (2007).
15. Kremer, J. *et al.* Measurements of ground-level muons at two geomagnetic locations. *Phys. Rev. Lett.* **83**, 4241 (1999).
16. Munakata, K. *et al.* Precursors of geomagnetic storms observed by the muon detector network. *J. Geophys. Res.* **105**, 27457–27468 (2000).
17. Olive, K. A., Group, P. D. *et al.* Review of particle physics. *Chin. Phys.* **C38**, 090001 (2014).
18. Dayananda, M., Zhang, X., Butler, C. & He, X. Understanding the effect of atmospheric density on the cosmic ray flux variations at the earth surface. *arXiv:1303.7191* (2013).
19. Sagisaka, S. Atmospheric effects on cosmic-ray muon intensities at deep underground depths. *Nuovo Cimento* **C9**, 809–828 (1986).
20. Motoki, M. *et al.* Precise measurements of atmospheric muon fluxes with the bess spectrometer. *Astropart. Phys.* **19**, 113–126 (2003).
21. Anchordoqui, L. *et al.* High energy physics in the atmosphere: Phenomenology of cosmic ray air showers. *Ann. Phys.* **314**, 145–207 (2004).
22. Blackett, P. M. On the instability of the barytron and the temperature effect of cosmic rays. *Phys. Rev.* **54**, 973 (1938).
23. Duperier, A. A new cosmic-ray recorder and the air-absorption and decay of particles. *Terrestr. Magnet. Atm. Electr.* **49**, 1–7 (1944).
24. Zazyan, M., Ganeva, M., Berkova, M., Yanke, V. & Hippler, R. Atmospheric effect corrections of mustang data. *J. Space Weather Space Clim.* **5**, A6 (2015).
25. Skellam, J. G. The frequency distribution of the difference between two poisson variates belonging to different populations. *J. Roy. Stat. Soc.* **A109**, 296–296 (1945).
26. Nagamine, K., Iwasaki, M., Shimomura, K. & Ishida, K. Method of probing inner-structure of geophysical substance with the horizontal cosmic-ray muons and possible application to volcanic eruption prediction. *Nucl. Instrum. Methods* **A356**, 585–595 (1995).
27. Hebbeker, T. & Timmermans, C. A compilation of high energy atmospheric muon data at sea level. *Astropart. Phys.* **18**, 107–127 (2002).
28. Tang, A., Horton-Smith, G., Kudryavtsev, V. A. & Tonazzo, A. Muon simulations for super-kamiokande, kamland, and chooz. *Phys. Rev.* **D74**, 053007 (2006).
29. Lesparre, N. *et al.* Design and operation of a field telescope for cosmic ray geophysical tomography. *Geosci. Instrum. Method Data Syst.* **1**, 33–42 (2012).
30. Marteau, J. *et al.* Implementation of sub-nanosecond time-to-digital convertor in field-programmable gate array: applications to time-of-flight analysis in muon radiography. *Meas. Sci. Technol.* **25**, 035101 (2014).
31. Ambrosio, M. *et al.* Seasonal variations in the underground muon intensity as seen by macro. *Astropart. Phys.* **7**, 109–124 (1997).
32. Adamson, P. *et al.* Observation of muon intensity variations by season with the minos far detector. *Phys. Rev.* **D81**, 012001 (2010).
33. Tilav, S. *et al.* Atmospheric variations as observed by icecube. *arXiv:1001.0776* (2010).
34. Poirier, J. & Catanach, T. Periodic variations in muon flux at project grand. In *Proc. Int. Cosmic Ray Conf.*, vol. 11, 173–176 (2011).
35. Heck, D., Schatz, G., Knapp, J., Thouw, T. & Capdevielle, J. Corsika: A monte carlo code to simulate extensive air showers. *Tech. Rep.* (1998).
36. Wentz, J. *et al.* Simulation of atmospheric muon and neutrino fluxes with corsika. *Phys. Rev.* **D67**, 073020 (2003).

## Acknowledgements

This study is part of the DIAPHANE project ANR-14-CE 04-0001. We acknowledge the financial support from the UnivEarthS Labex program of Sorbonne Paris Cité (ANR-10-LABX-0023 and ANR-11-IDEX-0005-02). We would like to thank also the members of the SIEPC, Tignieu-Jamezieu, France, for their help, support and the access to the data. In particular we thank Mr Gilbert Pommet and Mr Rémi Cachet. The results presented in this paper rely on geomagnetic Kp indices calculated and made available by ISGI Collaborating Institutes and on the data collected at Chambon-la-Forêt magnetic observatory. We thank the Institut de Physique du Globe de Paris, for supporting its operation and the INTERMAGNET network and ISGI (isgi.unistra.fr). This is IPGP contribution \*\*\*\*.

## Author contributions statement

K.J., J.M. and D.G. conceived the experiment; K.J., D.G., J.M., J.B.A., S.G., C.G. and J.C.I. designed and constructed the apparatus; K.J. and J.M. conducted the experiment; K.J., J.M., J.B.A. and D.G. analysed the data; K.J., J.M., J.B.A. and D.G. wrote the article.

## Additional information

**Competing financial interests:** The authors declare no competing financial interests.